ACS OMEGA

http://pubs.acs.org/journal/acsodf

Article

Synthesis of Highly Efficient and Recyclable Bimetallic Co_x–Fe_{1-x}–MOF for the Synthesis of Xanthan and Removal of Toxic Pb^{2+} and Cd^{2+} Ions

Mohammed A. Mannaa,* Mosaad R. Mlahi, A. AL Maofari, Awad I. Ahmed, and Shawky M. Hassan

Cite This: *ACS Omega* 2023, 8, 26379–26390

Read Online

ACCESS | Metrics & More | Article Recommendations | Supporting Information

ABSTRACT: Mono-(Fe) and bimetallic Co_x–Fe_{1-x}–MOF with different Co and Fe contents was successfully synthesized by the solvothermal method. The structural properties of the prepared samples were characterized by X-ray diffraction, transmission electron microscopy (TEM), Brunauer–Emmett–Teller specific surface area, and Fourier transform infrared spectroscopy. The results revealed the successful formation of mono and mixed Co_x–Fe_{1-x}–MOF. Also, the results of TEM displayed that the particle structure of Co_x–Fe_{1-x}–MOF changed to octahedral after the addition of cobalt. The surface acidity results illustrated that the samples showed both Lewis and Brønsted acid sites, and Co_x–Fe_{1-x}–MOF possessed more surface acidity than Fe–MOF. The catalytic performance of the prepared samples was tested by synthesis of 14-phenyl-14*H*-dibenzo [a, j] xanthene (xanthene), and bimetallic Co_x–Fe_{1-x}–MOF showed higher activity compared to monometallic Fe–MOF. The sample with $Co_{0.50}$–$Fe_{0.50}$–MOF gave the highest yield of xanthene with 90.2%. In addition, the prepared samples were used for removal of Pb^{2+} and Cd^{2+} ions from the aqueous solution. The sample with $Co_{0.50}$–$Fe_{0.50}$–MOF showed the highest removal efficiency compared with mono- and other bimetallic samples. The results illustrated that the addition of Co to Fe enhanced the structural properties, acidity, and catalytic performance of the prepared samples due to the synergistic effect between Fe and Co ions. According to the obtained results, the prepared samples showed great potentials for the synthesis of pharmacologically active compounds and environmental protection.

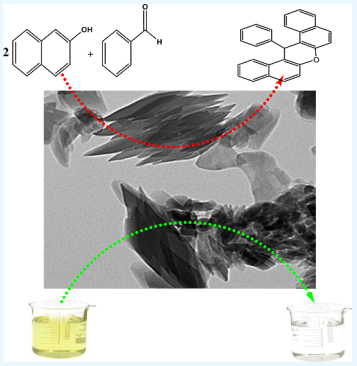

1. INTRODUCTION

In the last decade, metal–organic frameworks (MOFs) attracted more attention due to their unusual properties such as structural diversity, exceptional porosity, and different potential applications.[1−4] These unique properties of MOFs made these materials appropriate for widespread applications such as adsorption, separation, storage, sensors, magnetism, drug delivery, and catalysis.[5−7] Moreover, compared with conventionally micro/mesoporous inorganic materials, MOFs exhibited a more flexible rational design of their structure by controlling the synthesis approach and organic linker types.[8−10] Continual efforts have been exerted to develop the structural properties and potential applications of MOFs. One of these methods is the formation of mixed MOFs by combining two or more types of MOFs. Bimetallic MOFs exhibited excellent hydrostability and activity compared with monometallic MOFs.[10−13] Numerous MOFs have been applied as heterogeneous catalysts for liquid-phase reactions such as oxidative desulfurization,[14] hydroxyalkylation of phenol,[15] esterification reactions of hydrophilic alcohols,[16] etc. Xanthene derivatives have attracted more attention due to their importance in therapeutic, pharmaceutical, and biological features, like blood palette aggregation inhibitor drugs;[2] photodynamic therapy;[17] agricultural bactericide activity;[18] antibacterial, antiviral,[2] and anti-inflammatory activity; and antitumor activity.[19] Different methods have been reported for the synthesis of xanthene derivatives including using different catalysts such as sulfamic acid/MCM-41,[20] phosphated tin oxide,[21] $H_3PW_{12}O_{40}$/Sn–TiO_2,[22] cellulose sulfamic acid,[23] SnO_2/TiO_2,[24,25] and MCM-41 grafted with citric acid.[26]

Heavy metals became one of the dangerous environmental problems due to increasing the factories in recent years, which led to increase the concentrations of these toxic metals in water and wastewater.[27−29] Heavy metals such as Cr^{2+}, Cd^{2+}, Cu^{2+}, and Pb^{2+} are very toxic and introduce in ecosystems through industrial wastewaters during the chemical manufacturing, oil refining, alloy manufacturing, leather tanning, and battery manufacturing.[2,30] The dangerous effects of these metal ions on human beings' health and ecological systems resulted due to the biomagnification property of these metal ions in the human body throughout the food chain, causing a variety of diseases and disorders when the human is exposed to it for a long time.[2,30−32] So, it is important to eliminate the toxic

Received: April 27, 2023
Accepted: July 4, 2023
Published: July 15, 2023

metals that resulted from industrial wastewater before disposal to the environment. Different methods have been reported for the removal of these toxic metals including ion exchange, ultrafiltration,[30] adsorption,[33] reverse osmosis,[30] etc. However, the adsorption technique is considered one of the most preferred techniques due to its advantages as low cost, simplicity, and high efficiency.[34,35] Various materials have been applied as adsorbents for the removal of heavy metals such as modified MCM-41,[26] zeolite,[36] activated carbon,[37] etc. However, some weaknesses were observed after the application of these adsorbents. MOFs have been recently applied as efficient adsorbents for different pollutants due to their features like high surface area, tunable pore sizes and structure, and stability in aqueous media.[12] In addition, the tunability of their surface structure made these materials more important in different applications, especially as adsorbents of different pollutants.[2]

In this work, mixed-component metal−organic frameworks (Co_x−Fe_{1-x}−MOF) with different molar ratios of Co/Fe (0:1, 0.25:0.75, 0.50:0.50, and 0.75:0.25) were synthesized by a solvothermal approach. The prepared samples were applied as heterogeneous solid acid catalysts for the synthesis of 14-phenyl-14*H*-dibenzo[a, j]xanthene and removal of some heavy metals (Pb^{2+} and Cd^{2+} ions). The surface acidity and the types of acid sites [Lewis (L) and Brønsted (B)] were determined by potentiometric titration and chemisorbed of pyridine, respectively. The parameters that affect the activity of samples for the synthesis of xanthene and adsorption of Pb^{2+} and Cd^{2+} ions were investigated.

2. EXPERIMENTAL SECTION

2.1. Materials. Ferric nitrate pentahydrate [$Fe(NO_3)_3 \cdot 9H_2O$, 99%] and cobalt nitrate hexahydrate [$Co(NO_3)_2 \cdot 6H_2O$, 99% %] were obtained from Sigma-Aldrich. Terephthalic acid (1,4-BDC, 99%) was supplied from Sigma-Aldrich. *N*,*N*-Dimethylformamide (DMF, 99.5%), ethanol (99.5%), *N*-butylamine, acetonitrile, lead nitrate, cadmium chloride, *β*-naphthol benzaldehyde, HNO_3, and NaOH were supplied from Sigma-Aldrich and used as received.

2.2. Synthesis of (Co_x−Fe_{1-x}−MOF). Bimetallic metal−organic frameworks (Co_x−Fe_{1-x}−MOF) were synthesized via a solvothermal approach according to previous literature studies with slight modification:[12,38] A mixture of cobalt nitrate and iron(III) nitrate with different molar ratios (0.25:0.75, 0.50:0.50, and 0.75:0.25) was mixed with terephthalic acid and dissolved in DMF (40 mL) under continuous stirring for 1 h. The resulting homogeneous mixture was moved to a Teflon-lined steel autoclave and then transferred to an oven at 130 °C for 12 h. After that, the autoclave was left to cool, and the resultant precipitate was soaked in DMF for 1 day to remove the unreacted linker (BDC) captured inside the pores and then soaked in distilled water to remove any unreacted metal precursor loaded inside the pores. After filtration, the resultant MOF was dried at 100 °C for 3 h. Also, monometallic Fe−MOF was synthesized by the same procedure without adding the cobalt precursor.

2.3. Characterization Techniques. The powder X-ray diffraction (XRD) patterns of the prepared samples were recorded using a Philips X'Pert diffractometer under Cu K*α* radiation. The morphology of the prepared samples was measured by transmission electron microscopy (TEM, JEOL JEM-2100). Fourier transform infrared (FT-IR) spectra were examined using a Thermo SCIENTIFIC (NICOLET iS10) FTIR spectrophotometer. Brunauer−Emmett−Teller surface area (S_{BET}) and pore size distribution measurements were performed with N_2 adsorption isotherms using a BELSORP-mini II analyzer. Surface acidity was investigated by two methods, non-aqueous potentiometric titration using an Orion 420 digital model and FT-IR spectroscopy of chemisorbed pyridine.

2.4. Surface Acidity Measurements. *2.4.1. Non-aqueous Titration Method.* In this method, total acidity (total number of acid sites and acid strength) was achieved by potentiometric titration.[39] In the procedure, 0.05 g of the sample was activated and suspended in 10 mL of acetonitrile for 2 h. After that, the suspension was titrated with *n*-butylamine (0.1 N) in acetonitrile, and the titration rate was 0.05 mL/min. The variations in the potential values of the electrode were measured by an Orion 420 digital model.

2.4.2. Determine the Nature of Acid Sites. In this method, the nature of acid sites (B and/or L) on the surface of samples was examined by the FTIR spectra of chemisorbed pyridine.[20,26] In the procedure, the samples were activated at 150 °C for 2 h under vacuum, and then the activated samples were soaked in dried pyridine and left for 48 h. After that, the samples were evaporated at 100 °C to remove the excess pyridine.

2.5. Catalytic Activities. *2.5.1. Synthesis of Xanthene.* Generally, a mixture of 2-naphthol (2 mmol) and aldehyde (1 mmol) was stirred in a flask, and then 0.05 g of the catalyst was added. The resultant mixture was heated at 125 °C for a suitable time (completion of the reaction was monitored by thin-layer chromatography). After that, the resulting product was cooled to room temperature. The crude product was heated in chloroform, and then the used catalyst was filtered off. The resultant product was recrystallized in ethanol to form 14-phenyl-14*H*-dibenzo[a, j]xanthene, which is characterized by the melting point (182 °C) and FTIR spectrum. The yield percentage was calculated through the following relation

$$\text{Yield (wt\%)} = \left(\frac{\text{obtained weight of the product}}{\text{theoretical weight of the product}} \right) \times 100 \quad (1)$$

2.5.2. Adsorption Studies. The adsorption efficiency of Fe−MOF and Co_x−Fe_{100-x}−MOF was investigated by the addition of 0.03 g of sample into 100 mL of Pb^{2+} or Cd^{2+} ion solutions in Erlenmeyer flasks and then shaken for 2 h at 150 rpm and 25 °C. The pHs of Pb^{2+} and Cd^{2+} suspensions were adjusted to 5 and 7, respectively, by (0.1 M) HNO_3 and (0.1 M) NaOH. The concentrations of metal ions were measured using a UV−visible spectrophotometer. The effect of pH was studied in the range of 3−7 by adjusting with 0.1 M NaOH and 0.1 M HNO_3 solutions. The adsorption kinetics were carried out at the best conditions over the prepared MOFs.

The adsorption quantity of Pb^{2+} and Cd^{2+} ions at equilibrium [q_e ($mg.g^{-1}$)] was calculated from eq 2

$$q_e = \frac{(C_0 - C_e)\, V}{m} \quad (2)$$

where C_e and C_0 are the equilibrium and initial concentrations ($mg \cdot L^{-1}$) of metal ions, respectively. m is the sample weight (g) and V (L) is the solution volume.

https://doi.org/10.1021/acsomega.3c02911
ACS Omega 2023, 8, 26379−26390

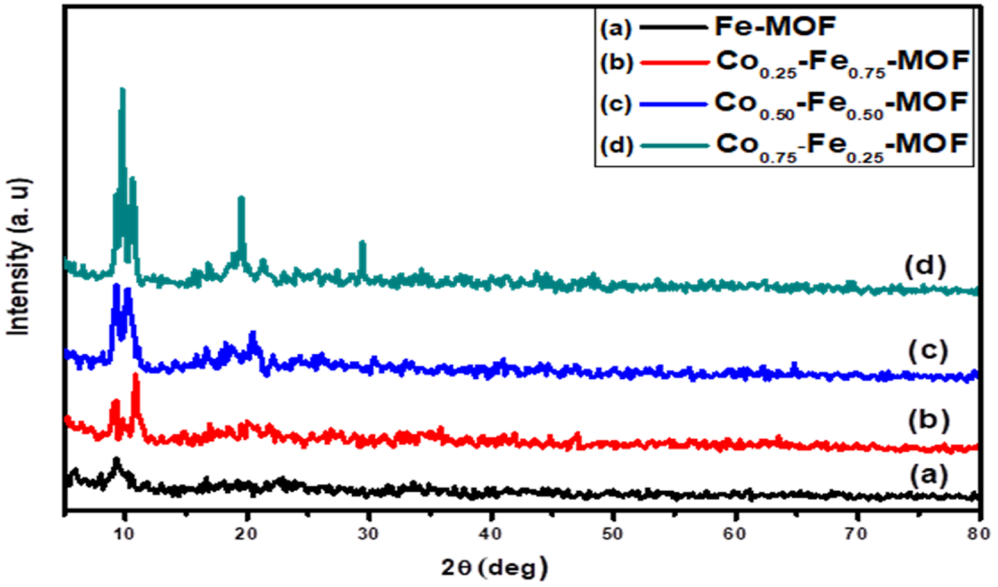

Figure 1. XRD spectra of Fe−MOF and Co_x−Fe_{1-x}−MOFs at different Co and Fe molar ratios.

3. RESULTS AND DISCUSSION

3.1. X-Ray Diffraction Analysis. The XRD patterns of monometallic Fe−MOF and Co_x−Fe_{1-x}−MOF with different molar ratios of Fe and Co ions are displayed in Figure 1. The XRD patterns of the monometallic sample showed peaks located at 2θ = 9.3, 10.2, 11.6, 12.8, 16.8, 18.2, 19.4, 20.3, 22.7, 29.3, 33.5, and 41.6°, which are in good agreement with the XRD patterns of pure Fe−MOF.[13,40−42] On the other hand, the XRD patterns of bimetallic Co_x−Fe_{1-x}−MOF showed similar diffraction peaks to Fe−MOF. In addition, new diffraction peaks were detected at 2θ = 9.7, 14.1, 15.8, 20.4, and 21.7° reflecting to Co−MOF.[13,43] However, new peaks were observed at 19.4, 44.4, and 69.1° with increasing cobalt content to $Co_{0.75}$−$Fe_{0.25}$−MOF, indicating the aggregation of cobalt oxide crystals on the surface of the sample.[44,45] Also, the positions of some peaks were changed with changed molar ratios of Co and Fe ions, especially the peak located at 10.2°, indicating the mutual effect of combination between Fe and Co ions with the linker.[13] It is worth noting that the intensity of peaks at 9.3, 9.8, and 10.2° increased after the addition of Co ions (Figure 1). Moreover, the intensity of the peak at 9.7° increased sharply in the case of $Co_{0.50}$−$Fe_{0.50}$−MOF, indicating the strong interactions between the metals and the linker, which may be resulted from the synergistic effect between Fe and Co ions. In addition, increasing the intensity of peaks in the case of $Co_{0.75}$−$Fe_{0.25}$−MOF compared with other samples indicates the well-developed crystallinity of $Co_{0.75}$−$Fe_{0.25}$−MOF.

3.2. TEM Analysis. The morphologies of mono- and bimetallic samples were investigated as displayed in Figure 2. The TEM images showed different shapes and particle sizes, indicating the effect of Fe:Co ratios on the structural and morphological properties of the samples. The TEM image showed that Fe−MOF has low crystallinity compared with other samples (Figure 2a). The TEM images of the bimetallic samples displayed that the crystallinity and regularity of shapes of particles improved after the addition of Co ions. Moreover, increasing the molar ratio of Co ions compared with Fe ions was accompanied by increasing the particle sizes (Figure 2b,d). The samples that have a molar ratio of 0.50:0.50 of Fe and Co ions showed needles and irregular octahedral shapes (Figure 2c). However, $Co_{0.75}$−$Fe_{0.25}$−MOF that has 0.75 molar ratio of cobalt displayed the best crystallites with regular octahedral shapes as displayed in Figure 2d. According to these results, we can conclude that the optimal molar ratios of Fe and Co ions that can be taken is 0.50:0.50, where at this ratio, the strongest interactions between these metal ions and the linker occurred and the preferred shapes of the particles can result.

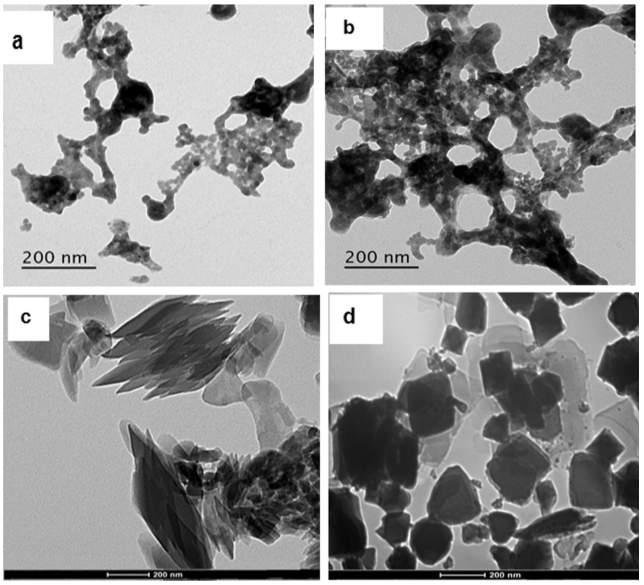

Figure 2. TEM images of (a) Fe−MOF, (b) $Co_{0.25}$−$Fe_{0.75}$−MOF, (c) $Co_{0.50}$−$Fe_{0.50}$−MOF, and (d) $Co_{0.75}$−$Fe_{0.25}$−MOF.

3.3. S_{BET} Measurements. The texture properties of Fe−MOF and Co_x−Fe_{1-x}−MOF samples have been investigated by N_2 adsorption−desorption isotherms as displayed in Figure 3. The samples showed type-IV isotherms with secondary two steep rises at the P/P_0 curve, indicating the existence of two types of pores, micro- and mesoporous.[14,46] The surface area (S_{BET}) and pore volume (V_{pore}) of the prepared samples were calculated, and the obtained values are listed in Table 1. From the obtained results in Table 1, the values of S_{BET} and V_{pore}

https://doi.org/10.1021/acsomega.3c02911
ACS Omega 2023, 8, 26379−26390

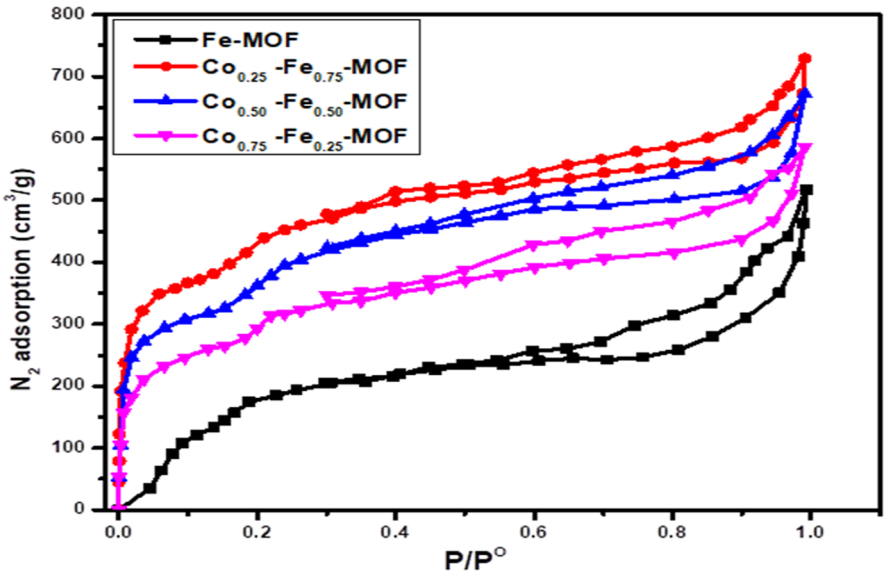

Figure 3. N_2 adsorption−desorption isotherm at 77 K for Fe−MOF and Co_x−Fe_{1-x}−MOFs at different Co and Fe molar ratios.

Table 1. Physicochemical Properties and Catalytic Activity of the Prepared Catalysts

sample	S_{BET} m^2/g	V_{pore} Cm^3/g	E_i (mV)	no. of acid sites/g × 10^{19}	L/B ratio	xanthene %
Fe−MIL101	924.2	0.545	140.34	9.64		81.5
$Co_{0.25}$−$Fe_{0.75}$−MOF	1283.3	0.834	275.12	12.05	0.70	86.8
$Co_{0.50}$−$Fe_{0.50}$−MOF	1104.8	0.802	310.2	13.85	1.07	90.2
$Co_{0.75}$−$Fe_{0.25}$−MOF	1017.6	0.681	250.76	10.84	1.20	91.5

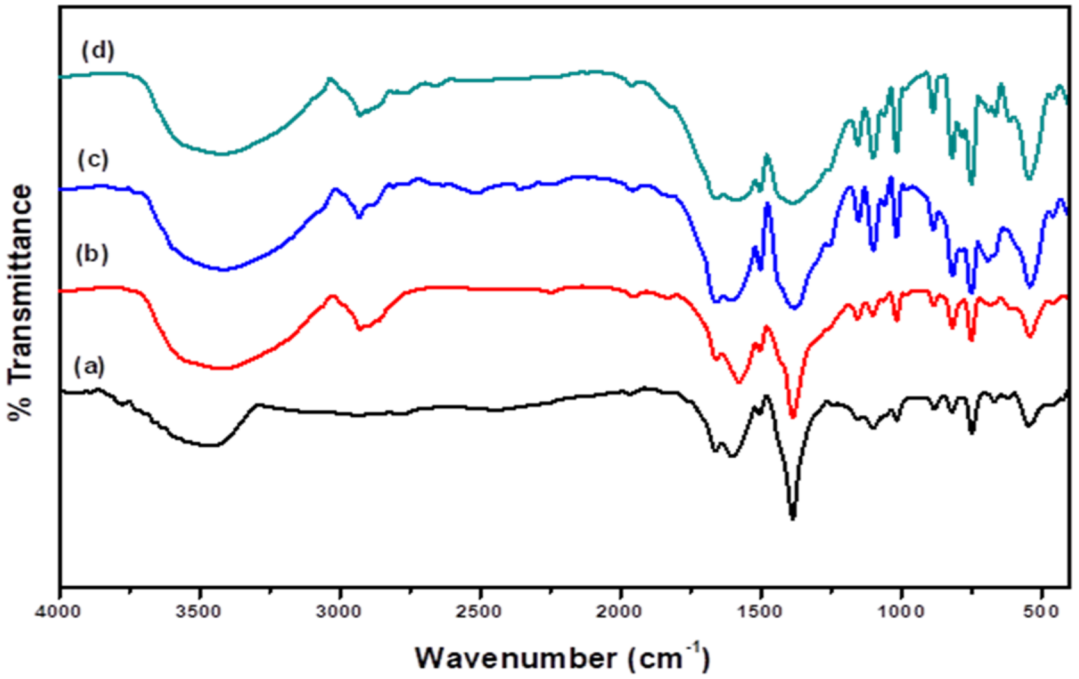

Figure 4. FTIR spectra of (a) Fe−MOF, (b) $Co_{0.25}$−$Fe_{0.75}$−MOF, (c) $Co_{0.50}$−$Fe_{0.50}$−MOF, and (d) $Co_{0.75}$−$Fe_{0.25}$−MOF.

increased after the addition of cobalt and the sample with $Co_{0.25}$−$Fe_{0.75}$−MOF showed the highest S_{BET} and V_{pore}, indicating that the existence of Co and Fe ions together in the same framework led to the creation of new pores and new active sites on the surface of samples leading to enhancement of S_{BET} and V_{pore}.[2] However, increasing the molar ratio of Co to 0.5 and 0.75 was accompanied by reduction in the S_{BET} and V_{pore}, indicating the aggregation of cobalt oxide crystals on the surface of Co_x−Fe_{1-x}−MOF. On the other hand, the size of crystals increased by increasing the ratio of cobalt, which in turn reduced the values of S_{BET} and V_{pore}. In addition, Figure S1 (Supporting Information) shows the pore size distribution curves of Fe−MOF and Co_x−Fe_{1-x}−MOF, where the samples displayed two different sizes of pores, 11.05 and 24.8 Å.

https://doi.org/10.1021/acsomega.3c02911
ACS Omega 2023, 8, 26379−26390

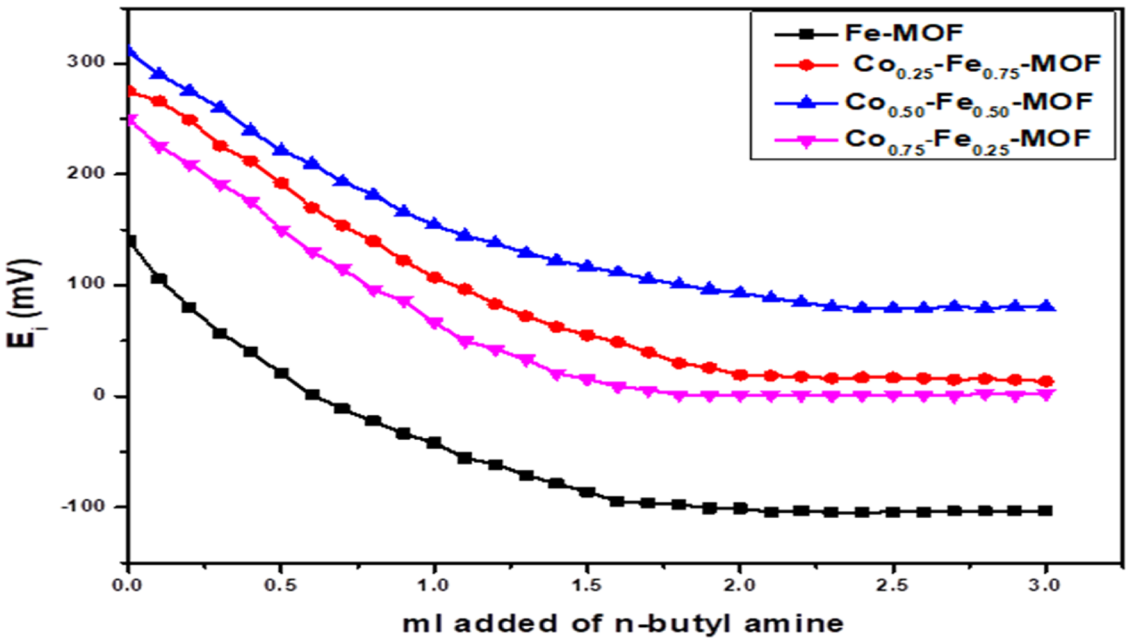

Figure 5. Potentiometric titration curves of Fe−MOF and Co_x−Fe_{1-x}−MOFs at different Co and Fe molar ratios.

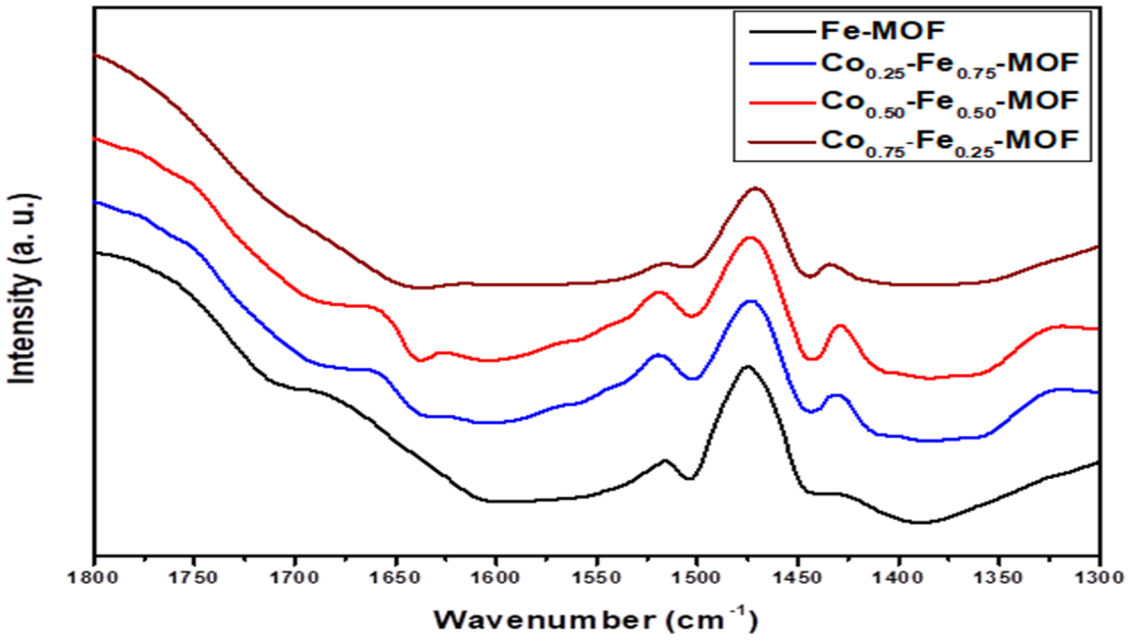

Figure 6. FTIR spectra of pyridine adsorbed over Fe−MOF and Co_x−Fe_{1-x}−MOFs.

Moreover, small shifts were observed toward the microporous side with increasing the molar ratio of Co, indicating the incorporation of a small amount of cobalt oxide crystals in the pores which in turn led to a slight decrease in the pore sizes.

3.4. FT-IR Analysis. The FTIR spectra of Fe−MOF and Co_x−Fe_{1-x}−MOF (Figure 4) displayed a broad band at ∼3450 cm^{-1} assigned to the ν(O−H) of water and/or hydroxyl groups.[12,47,48] Also, another band appeared at 2930 cm^{-1} attributed to the stretching vibrations of C−H. The main characteristic bands appeared at 1662 cm^{-1} assigned to the stretching vibration of C═O (−COOH) while the absorption bands in the range of 1600−700 cm^{-1} are related to the vibration modes of aromatic rings in the linker.[2,49−51] Also, the band that appeared at 1387 cm^{-1} related to the asymmetric stretching of (C−O).[7] On the other hand, the bands that appeared at 1155, 1102, 1062, 884, and 748 cm^{-1} can be attributed to (C−H) deformations of aromatic rings,[7,49] while the bands that appeared at 673 and 613 cm^{-1} ascribed to the bending modes of ($-COO^-$) groups in and out of the plane.[12,46,52] The characteristic bands that appeared in the area under 600 cm^{-1} were assigned to M−O (M = Fe &/or Co) vibrations.[7,12] It is remarkable to note that no absorption bands appeared in the range of 1705−1720 cm^{-1}, indicating the occurrence of deprotonation of all the carboxyl groups in the linker and no unreacted linker was remaindered on the surface and/or pores of the prepared samples.[7,12] Also, the positions of the bands were changed with the change in the

https://doi.org/10.1021/acsomega.3c02911
ACS Omega 2023, 8, 26379−26390

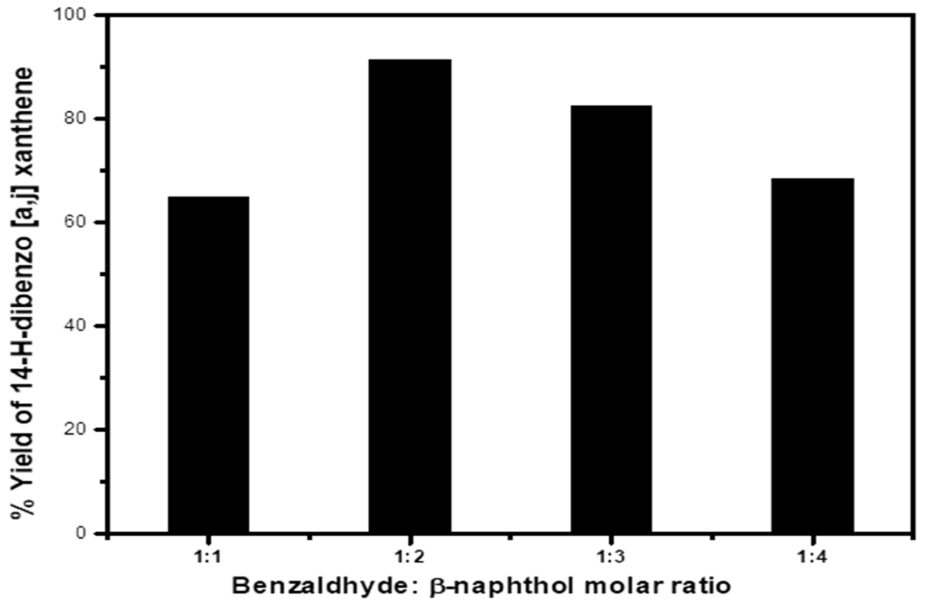

Figure 7. Effect of molar ratios of reactants on the yield percentage of xanthene.

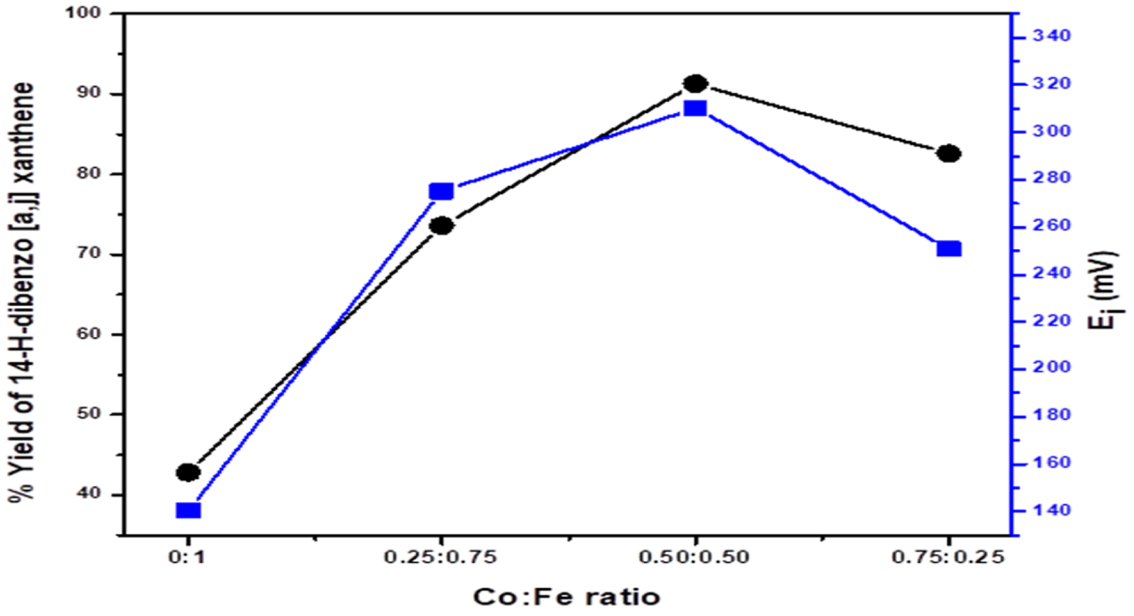

Figure 8. Effect of Co/Fe molar ratios on acid strength on the yield percentage of xanthene.

molar ratio of Fe and Co, which may be resulted due to the mutual effect between Fe and Co in the sample.

3.5. Surface Acidity Measurement. *3.5.1. Non-aqueous Titration.* The total acidity [acid strength and the total number of acid sites (T_{acs})] of the prepared samples was determined by the potentiometric titration method. The obtained curves are shown in Figure 5, and the calculated values of the acid strength and T_{acs} are listed in Table 1. The T_{acs} values were calculated from the following equation[22]

$$\text{Total no. of acid} \frac{\text{sites}}{g} = \frac{\text{steady point of plateau} \times m\text{equiv}\, g^{-1} \times N}{1000} \quad (3)$$

As shown in Table 1, the surface acidity (acid strength and T_{acs}) enhanced after the addition of cobalt compared with Fe–MOF, and the sample that has an equal molar ratio of $Co_{0.50}$–$Fe_{0.50}$–MOF showed the highest surface acidity. However, increasing the ratio of Co to 0.75 led to reducing the surface acidity. Based on these results, the surface acidity increase with increasing the ratio of Co compared with the monometallic sample may be ascribed to the role of cobalt in enhancing the acidity where the acidity improved after the addition of cobalt. Moreover, the role of synergistic effect between Co and Fe promoted the surface acidity of bimetallic samples.

3.5.2. Pyridine Adsorption. The types of acid sites (B and L) on the surface of samples can be determined efficiently using the adsorption of pyridine method. Figure 6 shows the FTIR spectra of pyridine adsorbed on the prepared samples. The samples showed typical bands at 1444 and 1638 cm^{-1}, where the absorption band at 1444 cm^{-1} is attributed to the coordinated pyridine to the Lewis acid sites (L), while the absorption band at 1638 cm^{-1} is assigned to the adsorption of

https://doi.org/10.1021/acsomega.3c02911
ACS Omega 2023, 8, 26379−26390

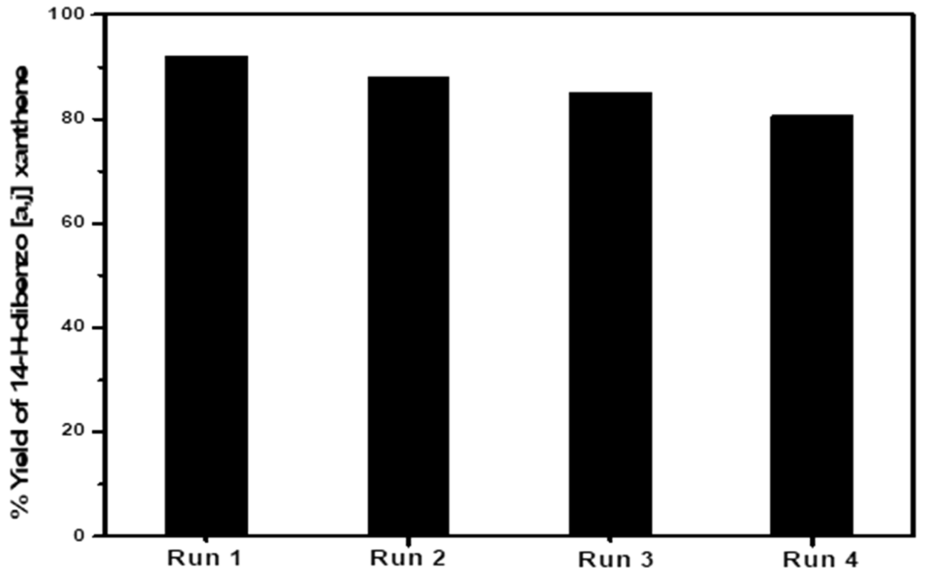

Figure 9. Effect of recycle times on the activity of $Co_{0.50}$−$Fe_{0.50}$−MOF for xanthene production.

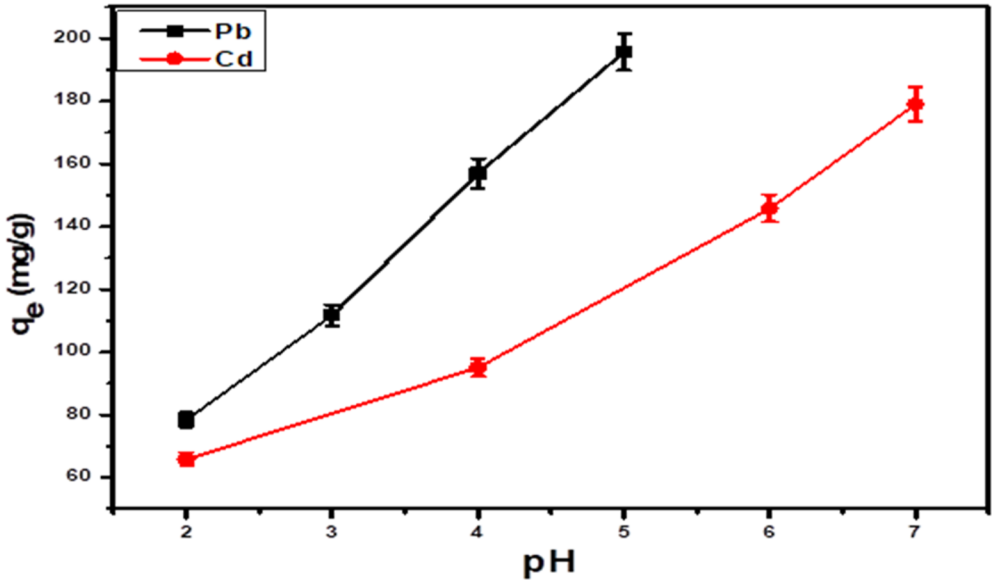

Figure 10. Effect of pH solution on the adsorption of Pb^{2+} and Cd^{2+} over $Co_{0.50}$−$Fe_{0.50}$−MOF.

pyridine at Brønsted acid sites (B).[21,22] The ratios of Lewis/Brønsted (L/B) acid sites were calculated from the integrated area of the peaks at 1444 cm^{-1} (L) and 1538 cm^{-1} (B). Figure 6 and Table 1 illustrate that Fe−MOF has only Lewis acid sites, while the bimetallic Co_x−Fe_{100-x}−MOF samples showed both L and B acid sites. The intensity of both L and B peaks was changed with the change in the molar ratios of Fe and Co in the samples. In addition, Table 1 displays that the L/B ratio increased with increasing the Co ratio, and the sample with $Co_{0.50}$−$Fe_{0.50}$−MOF gave the highest ratio of L/B. The enhancement in the number of sites of both L and B sites ascribes to the role of cobalt in the generation of new sites on the surface of samples. Also, the effect of synergistic between of two metals enhanced the strength acidity of these types. On the other hand, increasing the molar ratio of Co up to 0.75 was accompanied by reduction in the ratios of L/B.

3.6. Catalytic Activity. *3.6.1. Synthesis of 14-Aryl-14-H-dibenzo [a,j]xanthene. 3.6.1.1. Effect of Molar Ratio of the Reactants.* Figure 7 shows that the percentage of resulted xanthene depended on the molar ratio of the reactants. The reactions were achieved over $Co_{0.50}$−$Fe_{0.50}$−MOF under 120 °C. Different molar ratios were taken of Benzaldehyde: 2-naphthol (1:1, 1:2, and 1:3) under solvent-free conditions. Also, Figure 7 displays that the percentage of resulted xanthene increased with increasing the molar ratio up to 1:2 (benzaldehyde:β-naphthol). However, increasing the molar ratio to 1:3 was accompanied by decreasing the yield to 80%, indicating that the molar ratio at 1:2 is the most appropriate. The decrease in the yield percent at 1:3 resulted due to increasing the concentration of β-naphthol and worked in blocking of the active sites on the catalyst surface and consequently hindered the reaction.[22]

3.6.1.2. Effect of Co/Fe Ratio Content. Figure 8 illustrates the effect of Co/Fe molar ratios on the yield percentage of xanthene. Table 1 illustrates that the yield percentage of xanthene increased significantly after the addition of cobalt

https://doi.org/10.1021/acsomega.3c02911
ACS Omega 2023, 8, 26379−26390

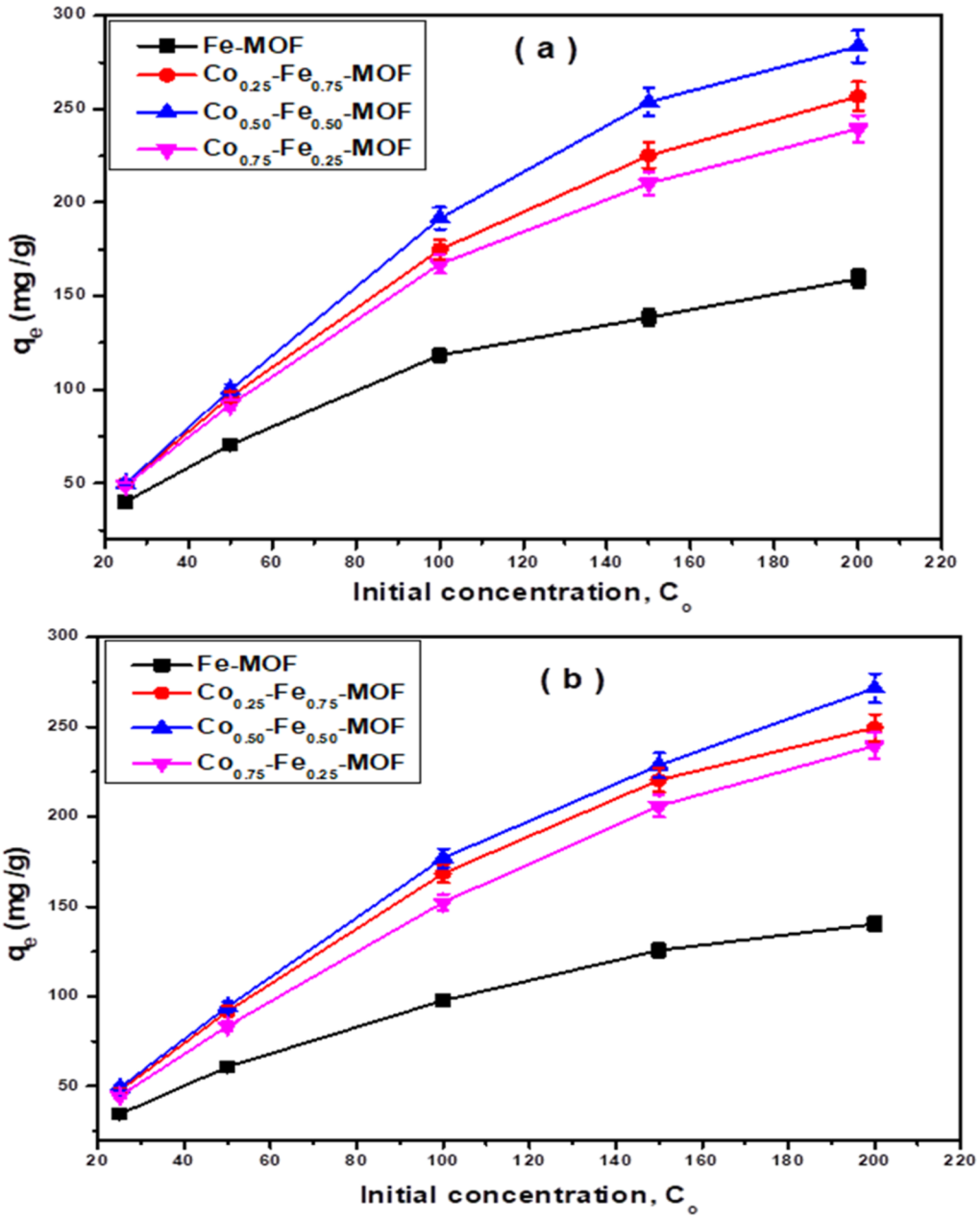

Figure 11. Effect of initial concentration of (a) Pb^{2+} and (b) Cd^{2+} on the removal efficiency of the prepared samples.

compared with monometallic Fe−MOF, indicating that the addition of cobalt enhanced the catalytic performance of Fe−MOF. Also, Figure 8 and Table 1 showed that the varying of molar ratios of Fe and Co in the sample affected the catalytic activity of the samples, where $Co_{0.50}$−$Fe_{0.50}$−MOF gave the highest yield of xanthene compared with the other molar ratios of Fe and Co, indicating that the best synergistic effect between the contents of the samples occurred at these molar ratios. Furthermore, Figure 8 and Table 1 display that the percent yield of xanthene increased in the same trend as the acid strength and L/B ratio. However, increasing the molar ratio of cobalt ($Co_{0.50}$−$Fe_{0.50}$−MOF) led to a decrease in the yield percent, which may be due to the accumulation of cobalt oxide crystals on the catalyst surface, which in turn led a reduction in the catalytic performance of $Co_{0.50}$−$Fe_{0.50}$−MOF toward xanthene production. Based on these results, the bimetallic samples showed remarkable catalytic performance compared with the monometallic sample.

3.6.1.3. Catalyst Reusability. The reusability of the prepared catalysts was investigated four cycles as shown in Figure 9. The reactions were carried out under the same condition over Co_{50}−Fe_{50}−MOF. After each cycle, the catalyst was retrieved by filtration, then washed with ethanol and deionized water, and finally reactivated in an oven at 120 °C. In addition, the effect of reuse times on the stability of the catalysts was investigated by XRD and FTIR analyses as shown in Figure S2. The results showed that no significant changes in the structural properties were detected after four cycles, indicating the high stability and excellent reusability of the prepared catalysts.

3.6.2. Adsorption of Pb^{2+} and Cd^{2+}. 3.6.2.1. Effect of pH. The pH of the solution is one of the important parameters that affect the adsorption activity of the adsorbent due to the

https://doi.org/10.1021/acsomega.3c02911
ACS Omega 2023, 8, 26379−26390

Table 2. Obtained Isotherm Parameters for Adsorption of Pb^{2+} and Cd^{2+} Ions over Fe−MOF and Co_x−Fe_{1-x}−MOFs

		Langmuir isotherm				Freundlich isotherm		
metal ion	sample	q_m (mg/g)	K_L (L/mg)	R^2	R_L	K_F (mg/g)	n	R^2
Pb^{2+}	Fe−MOF	120.8	0.06	0.9805	0.14	24.32	2.61	0.9926
	$Co_{0.25}$−$Fe_{0.75}$−MOF	179.2	0.26	0.9908	0.04	33.54	2.30	0.9231
	$Co_{0.50}$−$Fe_{0.50}$−MOF	198.6	0.44	0.9964	0.02	38.63	2.13	0.9183
	$Co_{0.75}$−$Fe_{0.25}$−MOF	169.3	0.16	0.9903	0.06	33.40	2.34	0.9231
Cd^{2+}	Fe−MOF	115.3	0.03	0.9974	0.33	12.9	1.97	0.9698
	$Co_{0.25}$−$Fe_{0.75}$−MOF	170.8	0.13	0.9956	0.08	49.9	2.49	0.9729
	$Co_{0.50}$−$Fe_{0.50}$−MOF	183.5	0.19	0.9851	0.05	70.2	2.99	0.9789
	$Co_{0.75}$−$Fe_{0.25}$−MOF	152.9	0.05	0.9905	0.20	28.2	1.99	0.9882

Table 3. Kinetic Parameters Obtained from the Pseudo-First-Order and Pseudo-Second-Order Fitting on the Adsorption Process of Pb^{2+} and Cd^{2+} over Fe−MOF and Co_x−Fe_{1-x}−MOFs

		$q_{e(Exp)}$ (mg/g)	pseudo-first-order			pseudo-second-order		
metal ions	sample		q_{e1} (mg/g)	K_1	R^2	q_{e2} (mg/g)	$K_2 \times 10^{-4}$	R^2
Pb^{2+}	Fe−MOF	118.4	220.17	0.025	0.9526	121.6	7.36	0.9891
	$Co_{0.25}$−$Fe_{0.75}$−MOF	177.5	302.48	0.036	0.9883	176.2	9.44	0.9926
	$Co_{0.50}$−$Fe_{0.50}$−MOF	193.4	358.53	0.041	0.9714	201.3	17.79	0.9968
	$Co_{0.75}$−$Fe_{0.25}$−MOF	168.1	404.64	0.033	0.9132	162.2	12.29	0.9929
Cd^{2+}	Fe−MOF	111.5	260.8	0.019	0.8382	123.1	3.6	0.9977
	$Co_{0.25}$−$Fe_{0.75}$−MOF	169.3	429.8	0.035	0.9659	187.2	83.6	0.9926
	$Co_{0.50}$−$Fe_{0.50}$−MOF	182.2	597.3	0.039	0.9713	195.3	92.9	0.9968
	$Co_{0.75}$−$Fe_{0.25}$−MOF	154.5	962.9	0.050	0.9715	172.1	1.6	0.9881

changes in the acid−base properties of the surface of the adsorbent.[2] Figure 10 illustrates the adsorption of Pb^{2+} and Cd^{2+} ions over $Co_{0.5}$−$Fe_{0.5}$−MOF. The removal of these ions was influenced by changing the pH of the solution and the highest removal efficiency over $Co_{0.50}$−$Fe_{0.50}$−MOF appeared at pH = 5.0 of Pb^{2+} and 7.0 in the case of Cd^{2+} (Figure 10). At low pH, the surface of the samples became more positive, and the function groups were protonated which caused more electrostatic repulsion between the surface of samples and Pb^{2+} and Cd^{2+} ions resulting in decreasing the removal of these metal ions. In addition, an excess of H_3O^+ was formed which in turn competed the metal ions on the surface of the adsorbent.[2,26] On the other hand, increasing the pH of the solution made the surface of samples more negatively charged due to the deprotonation of functional groups on the surface of samples and consequently enhanced the electrostatic attraction of cationic metal ions on the surface of samples.

3.6.2.2. Effect of Initial Pb^{2+} and Cd^{2+} Concentrations and Adsorption Isotherms. The removal capacity of Pb^{2+} and Cd^{2+} ions at different concentrations (25−200 mg/L) over the prepared samples is shown in Figure 11. It is clear that the removal amounts of both of Pb^{2+} and Cd^{2+} ions increased with increasing the initial concentrations up to 200 mg/L and then nearly steady constant (Figure 11). This may be due to the saturation of the adsorption sites on the samples. The bimetallic samples showed better adsorption capacity compared to the monometallic sample.

Langmuir and Freundlich adsorption isotherms were employed to analyze the equilibrium data and investigate the adsorption behavior of Pb^{2+} and Cd^{2+} ions over the surface of the prepared samples, and the equations of these models are represented as follows

$$\frac{C_e}{q_e} = \frac{1}{q_m k_l} + \frac{C_e}{q_m} \text{ (Langmuir model)} \quad (4)$$

$$\log q_e = \log K_F + \frac{1}{n}\log C_e \text{ (Freundlich model)} \quad (5)$$

where K_L and K_F are Freundlich and Langmuir constants, respectively, and q_m and n are the maximum adsorption capacity and adsorption intensity, respectively. Moreover, the dimensionless separation constant R_L is one of the main features of the Langmuir model, which is given from the below equation

$$R_L = \frac{1}{1 + K_L C_0} \quad (6)$$

The obtained isotherms are shown in Figures S3 and S4. The isotherm parameters and the correlation factor coefficients (R^2) were calculated and are listed in Table 2. From Table 2, the values of R^2 for the Langmuir model were higher than that calculated from the Freundlich model. Also, the values of maximum adsorption capacities (q_m) were in good agreement with the corresponding experimental values ($q_{e,EXP}$). Moreover, the obtained values of R_L were between 0 and 1, indicating that the adsorption process of Pb^{2+} and Cd^{2+} was favorable. Also, the obtained values of K_f and n are located between 0 and 1, indicating the high adsorption intensity as shown in Table 2. Based on these results, the Langmuir model is the more appropriate for describing the adsorption processes of both Pb^{2+} and Cd^{2+}. This indicates the homogeneity of sample surfaces and formation of monolayer adsorption on the surface of samples.

3.6.2.3. Effect of Contact Time. Figure S5 shows that the removal of Pb^{2+} and Cd^{2+} over Co_x−Fe_{1-x}−MOF increased with increasing the contact time for 240 min. Also, the figure depicts that bimetallic samples displayed more removal efficiency compared with monometallic samples, indicating that the addition of cobalt together with iron improved the adsorption activity of samples by generation of new sites on the surface of the samples. Also, Figure S5 shows that the efficiency

https://doi.org/10.1021/acsomega.3c02911
ACS Omega 2023, 8, 26379−26390

of samples for the removal of metal ions increased with increasing the molar ratio of cobalt and the sample with $Co_{0.5}$−$Fe_{0.5}$−MOF showed the highest removal efficiency compared with other molar ratios of Co/Fe. In addition, the removal rates of both Pb^{2+} and Cd^{2+} increased rapidly with time, and the adsorption reached equilibrium after 90 min.

3.6.2.4. Adsorption Kinetics. To study the adsorption mechanism, pseudo-first-order kinetic and pseudo-second-order kinetic models were applied as shown in Figures S6 and S7. The linear forms of the pseudo-first- (eq 7) and second (eq 8)-order models are expressed as follows

$$\ln(q_e - q_t) = \ln q_e - k_1 t \quad (7)$$

$$\frac{t}{q_t} = \frac{1}{k_2 q_e^2} + \frac{t}{q_e} \quad (8)$$

where q_e and q_t (mg/g) are the adsorption capacities of samples at equilibrium and after time (t), respectively. K_1 (min^{-1}) and K_2 (g/mg·min) are the rate constants of the pseudo-first- and second-order adsorption models. The adsorption kinetic parameters and R^2 were evaluated and are summarized in Table 3. As can be seen in this table, the calculated values of R^2 from the pseudo-second-order model were found to be closer to unity compared with that calculated from the pseudo-first-order model. In addition, the calculated values of adsorption capacities ($q_{e,cal}$) that obtained from the second-order model were in better agreement than that of the corresponding experimental values ($q_{e,EXP}$). According to these results, the pseudo-second-order model is more fitted to the obtained results and more appropriate for description of the adsorption behaviors of Pb^{2+} and Cd^{2+} ions over the prepared samples.

To investigate the activity of our samples toward removal of Pb^{2+} and Cd^{2+} from wastewater, we compared our results with those previously reported works.[2,53−57] From Table S1 (Supporting Information), it can be observed that Co_x−Fe_{1-x}−MOF showed excellent adsorption capacity compared with other literature studies for adsorption of Pb^{2+} and Cd^{2+}. This indicates that the prepared samples can be applied as efficient adsorbents for the treatment of wastewater and removal of heavy metals.

4. CONCLUSIONS

Monometallic and bimetallic (Co−Fe) MOFs with different Co/Fe ratios were successfully synthesized. TEM results displayed that the ratio of cobalt in the sample affects the particle size. The molar ratio of CO/Fe in the samples played the important role of influencing the sample properties. The prepared samples were applied for the synthesis of xanthene and removal of Pb^{2+} and Cd^{2+} ions. The samples showed high activity for the production of xanthene and removal of Pb^{2+} and Cd^{2+} ions. It is noted that the bimetallic MOFs showed more surface acidity and activity compared to monometallic MOFs. Moreover, the surface acidity, catalytic activity, and adsorption efficiency of bimetallic MOFs depend on the molar ratios between Co and Fe where both acidity and activity enhanced with increasing the cobalt ratio, and the optimum molar ratio was $Co_{0.50}$−$Fe_{0.50}$−MOF. Langmuir and Freundlich models were applied to study the adsorption isotherms, and the obtained data were fitted with the Langmuir model. Also, the adsorption kinetics results obeyed the pseudo-second-order model. The reusability and stability of the prepared samples were investigated for four cycles, and no significant loss in the activity was detected, indicating that the prepared samples possess high stability and reusability.

ASSOCIATED CONTENT

Supporting Information

The Supporting Information is available free of charge at https://pubs.acs.org/doi/10.1021/acsomega.3c02911.

Pore size distribution curves of Fe−MOF and Co_x−Fe_{1-x}−MOFs at different Co and Fe molar ratios, FTIR and XRD analysis of fresh and reused sample after four cycles, adsorption isotherms of Pb^{2+} and Cd^{2+} over Co_x−Fe_{1-x}−MOFs, effect of time on the adsorption of Pb^{2+} and Cd^{2+} ions, pseudo-first- and second-order kinetic plots of Pb^{2+} and Cd^{2+}, and comparison table of the adsorption efficiency of our samples with the previously reported articles (PDF)

AUTHOR INFORMATION

Corresponding Author

Mohammed A. Mannaa − *Chemistry Department, Faculty of Applied Science, Sa'adah University, Sa'adah 37970, Yemen;* orcid.org/0000-0001-7913-5925; Email: mnnaam@yahoo.com

Authors

Mosaad R. Mlahi − *Chemistry Department, Faculty of Applied Science, Sa'adah University, Sa'adah 37970, Yemen*

A. AL Maofari − *Chemistry Department, Faculty of Applied Science, Sa'adah University, Sa'adah 37970, Yemen*

Awad I. Ahmed − *Chemistry Department, Faculty of Science, Mansoura University, Mansoura 8080, Egypt*

Shawky M. Hassan − *Chemistry Department, Faculty of Science, Mansoura University, Mansoura 8080, Egypt*

Complete contact information is available at: https://pubs.acs.org/10.1021/acsomega.3c02911

Funding

This work did not receive any support, and no funding was received for this work.

Notes

The authors declare no competing financial interest.

REFERENCES

(1) Altass, H. M.; Morad, M.; Khder, A. E. R. S.; Mannaa, M. A.; Jassas, R. S.; Alsimaree, A. A.; Ahmed, S. A.; Salama, R. S. Enhanced Catalytic Activity for CO Oxidation by Highly Active Pd Nanoparticles Supported on Reduced Graphene Oxide /Copper Metal Organic Framework. *J. Taiwan Inst. Chem. Eng.* **2021**, *128*, 194−208.

(2) Abo El-Yazeed, W. S.; Abou El-Reash, Y. G.; Elatwy, L. A.; Ahmed, A. I. Facile Fabrication of Bimetallic Fe-Mg MOF for the Synthesis of Xanthenes and Removal of Heavy Metal Ions. *RSC Adv.* **2020**, *10*, 9693−9703.

(3) Zhu, W.; Wang, J.; Wu, D.; Li, X.; Luo, Y.; Han, C.; Ma, W.; He, S. Investigating the Heavy Metal Adsorption of Mesoporous Silica Materials Prepared by Microwave Synthesis. *Nanoscale Res. Lett.* **2017**, *12*, 323.

(4) Shi, J.; Wang, S.; Wang, M.; Wang, X.; Li, W. Robust Salen-Typed Ce-MOFs Supported Fe(III) Catalyst Fabricated by Metalloligand Strategy for Catalytic Epoxides with Alcohols. *Mol. Catal.* **2022**, *533*, 112764.

(5) Beg, S.; Rahman, M.; Jain, A.; Saini, S.; Midoux, P.; Pichon, C.; Ahmad, F. J.; Akhter, S. Nanoporous Metal Organic Frameworks as

Hybrid Polymer−metal Composites for Drug Delivery and Biomedical Applications. *Drug Discov. Today* **2017**, *22*, 625−637.
(6) Khder, A. E. R. S.; Hassan, H. M. A.; El-Shall, M. S. Metal-Organic Frameworks with High Tungstophosphoric Acid Loadingas Heterogeneous Acid Catalysts. *Appl. Catal., A* **2014**, *487*, 110−118.
(7) Salama, R. S.; Mannaa, M. A.; Altass, H. M.; Ibrahim, A. A.; Khder, A. E. R. S. Palladium Supported on Mixed-Metal-Organic Framework (Co-Mn-MOF-74) for Efficient Catalytic Oxidation of CO. *RSC Adv.* **2021**, *11*, 4318−4326.
(8) Solovyeva, M. V.; Gordeeva, L. G.; Aristov, Y. I. MIL-101(Cr)−methanol" as Working Pair for Adsorption Heat Transformation Cycles: Adsorbent Shaping, Adsorption Equilibrium and Dynamics. *Energy Convers. Manage.* **2019**, *182*, 299−306.
(9) Liu, D.; Lang, F. F.; Zhou, X.; Ren, Z. G.; Young, D. J.; Lang, J. P. A Cationic Coordination Polymer and Its Orange II Anion-Exchanged Products: Isolation, Structural Characterization, Photocurrent Responses, and Dielectric Properties. *Inorg. Chem.* **2017**, *56*, 12542−12550.
(10) Chołuj, A.; Zieliński, A.; Grela, K.; Chmielewski, M. J. Metathesis@MOF: Simple and Robust Immobilization of Olefin Metathesis Catalysts inside (Al)MIL-101-NH_2. *ACS Catal.* **2016**, *6*, 6343−6349.
(11) Perman, J. A.; Chen, M.; Mikhail, A. A.; Niu, Z.; Ma, S. Acid-Base Directed Supramolecular Isomers of Isophthalate Based MOFs for CO_2 Adsorption and Transformation. *CrystEngComm* **2017**, *19*, 4171−4174.
(12) Salama, R. S.; Hassan, S. M.; Ahmed, A. I.; El-Yazeed, W. S. A.; Mannaa, M. A. The Role of PMA in Enhancing the Surface Acidity and Catalytic Activity of a Bimetallic Cr-Mg-MOF and Its Applications for Synthesis of Coumarin and Dihydropyrimidinone Derivatives. *RSC Adv.* **2020**, *10*, 21115−21128.
(13) El-Dafrawy, S. M.; Salama, R. S.; El-Hakam, S. A.; Samra, S. E. Bimetal-organic frameworks (Cu -Cr −MOF) as a stable and efficient catalyst for synthesis of 3, 4-dihydropyrimidin-2-one and 14-phenyl-14H-dibenzo [a, j] xanthene. *J. Mater. Res. Technol.* **2020**, *9*, 1998−2008.
(14) Sun, M.; Chen, W. C.; Zhao, L.; Wang, X. L.; Su, Z. M. A PTA@MIL-101(Cr)-Diatomite Composite as Catalyst for Efficient Oxidative Desulfurization. *Inorg. Chem. Commun.* **2018**, *87*, 30−35.
(15) Xia, X.; Xu, Y.; Chen, Y.; Liu, Y.; Lu, Y.; Shao, L. Fabrication of MIL-101(Cr/Al) with Flower-like Morphology and Its Catalytic Performance. *Appl. Catal., A* **2018**, *559*, 138−145.
(16) Alavijeh, M. K.; Amini, M. M. Synthesis and Characterization of Butylamine-Functionalized Cr(III)−MOF−SO_3H: Synergistic Effect of the Hydrophobic Moiety on Cr(III)−MOF−SO_3H in Esterification Reactions. *Polyhedron* **2019**, *173*, 114142.
(17) Dabiri, M.; Baghbanzadeh, M.; Nikcheh, M. S.; Arzroomchilar, E. Eco-Friendly and Efficient One-Pot Synthesis of Alkyl-or Aryl-14H-Dibenzo [A, J] Xanthenes in Water. *Bioorg. Med. Chem. Lett.* **2008**, *18*, 436−438.
(18) Reddi Mohan Naidu, K.; Satheesh Krishna, B.; Anil Kumar, M.; Arulselvan, P.; Ibrahim Khalivulla, S.; Lasekan, O. Design, Synthesis and Antiviral Potential of 14-Aryl/heteroaryl-14H- Dibenzo[a, J]xanthenes Using an Efficient Polymer-Supported Catalyst. *Molecules* **2012**, *17*, 7543−7555.
(19) Nile, S. H.; Ko, E. Y.; Kim, D. H.; Keum, Y. S. Screening of Ferulic Acid Related Compounds as Inhibitors of Xanthine Oxidase and Cyclooxygenase-2 with Anti-Inflammatory Activity. *Rev. Bras. Farmacogn.* **2016**, *26*, 50−55.
(20) Salama, R. S.; El-Bahy, S. M.; Mannaa, M. A. Sulfamic Acid Supported on Mesoporous MCM-41 as a Novel, Efficient and Reusable Heterogenous Solid Acid Catalyst for Synthesis of Xanthene, Dihydropyrimidinone and Coumarin Derivatives. *Colloids Surf., A* **2021**, *628*, 127261.
(21) Hassan, S. M. H.; Mannaa, M. A.; Ibrahim, A. A. Nano-Sized Mesoporous Phosphated Tin Oxide as an Efficient Solid Acid Catalyst. *RSC Adv.* **2019**, *9*, 810−818.
(22) Hassan, S. M.; Ahmed, A. I.; Mannaa, M. A. Surface Acidity, Catalytic and Photocatalytic Activities of New Type $H_3PW_{12}O_{40}$/Sn-TiO_2 Nanoparticles. *Colloids Surf., A* **2019**, *577*, 147−157.
(23) Moradi, L.; Mirzaei, M. Immobilization of Lewis Acidic Ionic Liquid on Perlite Nanoparticle Surfaces as a Highly Efficient Solid Acid Catalyst for the Solvent-Free Synthesis of Xanthene Derivatives. *RSC Adv.* **2019**, *9*, 19940−19948.
(24) Hassan, S. M.; Ahmed, A. I.; Mannaa, M. A. Structural, Photocatalytic, Biological and Catalytic Properties of SnO_2/TiO_2 Nanoparticles. *Ceram. Int.* **2018**, *44*, 6201−6211.
(25) Hassan, S. M.; Ahmed, A. I.; Mannaa, M. A. Preparation and Characterization of SnO_2 Doped TiO_2 Nanoparticles: Effect of Phase Changes on the Photocatalytic and Catalytic Activity. *J. Sci.: Adv. Mater. Devices* **2019**, *4*, 400−412.
(26) A Mannaa, M.; Altass, H. M.; Salama, R. S.; Salama, R. S. MCM-41 Grafted with Citric Acid: The Role of Carboxylic Groups in Enhancing the Synthesis of Xanthenes and Removal of Heavy Metal Ions. *Environ. Nanotechnol., Monit. Manage.* **2021**, *15*, 100410.
(27) Qian, C.; Yin, J.; Zhao, J.; Li, X.; Wang, S.; Bai, Z.; Jiao, T. Facile Preparation and Highly Efficient Photodegradation Performances of Self-Assembled Artemia Eggshell-ZnO Nanocomposites for Wastewater Treatment. *Colloids Surf., A* **2021**, *610*, 125752.
(28) Núñez, R.; García, M. Á.; Alonso, J.; Melgar, M. J. Arsenic, Cadmium and Lead in Fresh and Processed Tuna Marketed in Galicia (NW Spain): Risk Assessment of Dietary Exposure. *Sci. Total Environ.* **2018**, *627*, 322−331.
(29) Borges, F. C.; Du, Z.; Xie, Q.; Trierweiler, J. O.; Cheng, Y.; Wan, Y.; Liu, Y.; Zhu, R.; Lin, X.; Chen, P.; Ruan, R. Fast Microwave Assisted Pyrolysis of Biomass Using Microwave Absorbent. *Bioresour. Technol.* **2014**, *156*, 267−274.
(30) Samiey, B.; Cheng, C.-H.; Wu, J. Organic-Inorganic Hybrid Polymers as Adsorbents for Removal of Heavy Metal Ions from Solutions: A Review. *Materials* **2014**, *7*, 673−726.
(31) Wang, K.; Tao, X.; Xu, J.; Yin, N. Novel Chitosan-MOF Composite Adsorbent for the Removal of Heavy Metal Ions. *Chem. Lett.* **2016**, *45*, 1365−1368.
(32) Liu, X.; Tang, J.; Fu, L.; Wang, H.; Wang, S.; Xiong, C.; Wang, S.; Zhang, L. Ligand Design of a Novel Metal-Organic Framework for Selective Capturing of Pb(II) from Wastewater. *J. Cleaner Prod.* **2023**, *386*, 135841.
(33) Liu, X.; Fu, L.; Liu, H.; Zhang, D.; Xiong, C.; Wang, S.; Zhang, L. Design of Zr - MOFs by Introducing Multiple Ligands for Efficient and Selective Capturing of Pb (II) from Aqueous Solutions. *ACS Appl. Mater. Interfaces* **2023**, *15*, 5974−5989.
(34) Fu, L.; Wang, S.; Lin, G.; Zhang, L.; Liu, Q.; Fang, J.; Wei, C.; Liu, G. Post-Functionalization of UiO-66-NH_2 by 2,5-Dimercapto-1,3,4-Thiadiazole for the High Efficient Removal of Hg(II) in Water. *J. Hazard. Mater.* **2019**, *368*, 42−51.
(35) Fu, L.; Wang, S.; Lin, G.; Zhang, L.; Liu, Q.; Zhou, H.; Kang, C.; Wan, S.; Li, H.; Wen, S. Post-Modification of UiO-66-NH_2 by Resorcyl Aldehyde for Selective Removal of Pb(II)in Aqueous Media. *J. Cleaner Prod.* **2019**, *229*, 470−479.
(36) Zhao, Y.; Fang, F.; Xiao, H. M.; Feng, Q. P.; Xiong, L. Y.; Fu, S. Y. Preparation of Pore-Size Controllable Activated Carbon Fibers from Bamboo Fibers with Superior Performance for Xenon Storage. *Chem. Eng. J.* **2015**, *270*, 528−534.
(37) Mena Aguilar, K. M.; Amano, Y.; Machida, M. Ammonium Persulfate Oxidized Activated Carbon Fiber as a High Capacity Adsorbent for Aqueous Pb(II). *J. Environ. Chem. Eng.* **2016**, *4*, 4644−4652.
(38) Mannaa, M. A.; Qasim, K. F.; Alshorifi, F. T.; El-Bahy, S. M.; Salama, R. S. Role of NiO Nanoparticles in Enhancing Structure Properties of TiO_2 and Its Applications in Photodegradation and Hydrogen Evolution. *ACS Omega* **2021**, *6*, 30386−30400.
(39) Ibrahim, A. A.; Hassan, S. M.; Mannaa, M. A. Mesoporous Tin Oxide-Supported Phosphomolybdic Acid as High Performance Acid Catalysts for the Synthesis of Hydroquinone Diacetate. *Colloids Surf., A* **2020**, *586*, 124248.

https://doi.org/10.1021/acsomega.3c02911
ACS Omega 2023, 8, 26379−26390

(40) Abutalib, M. M.; Alghamdi, H. M.; Rajeh, A.; Nur, O.; Hezmad, A. M.; Mannaa, M. A. Preparation of rGO/$FeMoO_4$ as High-Performance Photocatalyst for Degradation of Malachite Green, Phenol and H2 Evolution under Natural Sunlight. *Int. J. Hydrogen Energy* **2022**, *47*, 32955−32968.
(41) Chen, M. L.; Zhou, S. Y.; Xu, Z.; Ding, L.; Cheng, Y. H. Metal-Organic Frameworks of MIL-100(Fe, Cr) and MIL-101(Cr) for Aromatic Amines Adsorption from Aqueous Solutions. *Molecules* **2019**, *24*, 3718.
(42) Farisabadi, A.; Moradi, M.; Hajati, S.; Kiani, M. A.; Espinos, J. P. Controlled Thermolysis of MIL-101(Fe, Cr) for Synthesis of Fe X O Y /porous Carbon as Negative Electrode and Cr_2O_3/porous Carbon as Positive Electrode of Supercapacitor. *Appl. Surf. Sci.* **2019**, *469*, 192−203.
(43) Abutalib, M. M.; Alghamdi, H. M.; Rajeh, A.; Nur, O.; Hezma, A. M.; Mannaa, M. A. Fe_3O_4/Co_3O_4-TiO_2 S-Scheme Photocatalyst for Degradation of Organic Pollutants and H2production under Natural Sunlight. *J. Mater. Res. Technol.* **2022**, *20*, 1043−1056.
(44) Habib Ur Rehman, M.; Noor, T.; Iqbal, N. Effect of Zirconia on Hydrothermally Synthesized Co_3O_4/TiO_2 Catalyst for NOx Reduction from Engine Emissions. *Catalysts* **2020**, *10*, 209.
(45) Mohamed Reda, G.; Fan, H.; Tian, H. Room-Temperature Solid State Synthesis of Co_3O_4/ZnO P−n Heterostructure and Its Photocatalytic Activity. *Adv. Powder Technol.* **2017**, *28*, 953−963.
(46) Cabello, C. P.; Berlier, G.; Magnacca, G.; Rumori, P.; Palomino, G. T. Enhanced CO_2 Adsorption Capacity of Amine-Functionalized MIL-100(Cr) Metal-Organic Frameworks. *CrystEngComm* **2015**, *17*, 430−437.
(47) Alsulami, Q. A.; Rajeh, A.; Mannaa, M. A.; Albukhari, S. M.; Baamer, D. F. One-Step Preparation of RGO/Fe3O4−$FeVO_4$ Nanocomposites as Highly Effective Photocatalysts under Natural Sunlight Illumination. *Sci. Rep.* **2022**, *12*, 6565−6612.
(48) Liu, L.; Tai, X.; Zhou, X.; Liu, L. Synthesis, Post-Modification and Catalytic Properties of Metal-Organic Framework NH_2-MIL-53(Al). *Chem. Res. Chin. Univ.* **2017**, *33*, 231−238.
(49) Hashemzadeh, A.; Amini, M. M.; Tayebee, R.; Sadeghian, A.; Durndell, L. J.; Isaacs, M. A.; Osatiashtiani, A.; Parlett, C. M. A.; Lee, A. F. A Magnetically-Separable $H_3PW_{12}O_{40}$@Fe_3O_4/EN-MIL-101 Catalyst for the One-Pot Solventless Synthesis of 2H-indazolo[2,1-B] Phthalazine-Triones. *Mol. Catal.* **2017**, *440*, 96−106.
(50) Liu, Q.; Ning, L.; Zheng, S.; Tao, M.; Shi, Y.; He, Y. Adsorption of Carbon Dioxide by MIL-101(Cr): Regeneration Conditions and Influence of Flue Gas Contaminants. *Sci. Rep.* **2013**, *3*, 2916.
(51) Hassan, H. M. A.; Betiha, M. A.; Mohamed, S. K.; El-Sharkawy, E. A.; Ahmed, E. A. Stable and Recyclable MIL-101(Cr)−Ionic Liquid Based Hybrid Nanomaterials as Heterogeneous Catalyst. *J. Mol. Liq.* **2017**, *236*, 385−394.
(52) Alsulami, Q. A.; Rajeh, A.; Mannaa, M. A.; Albukhari, S. M.; Baamer, D. F. Preparation of Highly Efficient Sunlight Driven Photodegradation of Some Organic Pollutants and H2 Evolution over rGO/$FeVO_4$ Nanocomposites. *Int. J. Hydrogen Energy* **2021**, *46*, 27349−27363.
(53) Wang, K.; Gu, J.; Yin, N. Efficient Removal of Pb(II) and Cd(II) Using NH2-Functionalized Zr-MOFs via Rapid Microwave-Promoted Synthesis. *Ind. Eng. Chem. Res.* **2017**, *56*, 1880−1887.
(54) Chen, Y.; Chen, Z.; Yuan, L.; Xiao, Y.; Zhang, S. H.; Li, N. Adsorption of PO_4^{3-}, Cd(II), Pb(II), Cu(II), As(III), and As(V) Using a Carbonised Mn-Based Metal−organic Framework. *Arab. J. Chem.* **2023**, *16*, 104950.
(55) Zou, F.; Yu, R.; Li, R.; Li, W. Microwave-Assisted Synthesis of HKUST-1 and Functionalized HKUST-1-@$H_3PW_{12}O_{40}$: Selective Adsorption of Heavy Metal Ions in Water Analyzed with Synchrotron Radiation. *ChemPhysChem* **2013**, *14*, 2825−2832.
(56) Zhang, B.-L.; Qiu, W.; Wang, P.-P.; Liu, Y.-L.; Zou, J.; Wang, L.; Ma, J. Mechanism Study about the Adsorption of Pb(II) and Cd(II) with Iron-Trimesic Metal-Organic Frameworks. *Chem. Eng. J.* **2020**, *385*, 123507.
(57) Lei, C.; Gao, J.; Ren, W.; Xie, Y.; Abdalkarim, S. Y. H.; Wang, S.; Ni, Q.; Yao, J. Fabrication of Metal-Organic Frameworks @ Cellulose Aerogels Composite Materials for Removal of Heavy Metal Ions in Water. *Carbohydr. Polym.* **2019**, *205*, 35−41.

https://doi.org/10.1021/acsomega.3c02911
ACS Omega 2023, 8, 26379−26390